Ionospheric compensation in L-band InSAR time-series: Performance evaluation for slow deformation contexts in equatorial regions

Léo Marconato, Marie-Pierre Doin, Laurence Audin, Erwan Pathier

Science of Remote Sensing 9 (2024) 100113

Contents lists available at ScienceDirect

Science of Remote Sensing

journal homepage: www.sciencedirect.com/journal/science-of-remote-sensing

Ionospheric compensation in L-band InSAR time-series: Performance evaluation for slow deformation contexts in equatorial regions

Léo Marconato [a,*], Marie-Pierre Doin [a], Laurence Audin [a], Erwan Pathier [a]

[a] Univ. Grenoble Alpes, Univ. Savoie Mont Blanc, CNRS, IRD, Univ. Gustave Eiffel, ISTerre, 38000, Grenoble, France

ARTICLE INFO

Keywords:
Synthetic aperture radar SAR interferometry
range split spectrum
Ionospheric effect
Ionospheric correction
Time-series analysis

ABSTRACT

Multi-temporal Synthetic Aperture Radar Interferometry (MT-InSAR) is the only geodetic technique allowing to measure ground deformation down to mm/yr over continuous areas. Vegetation cover in equatorial regions favors the use of L-band SAR data to improve interferometric coherence. However, the electron content of ionosphere, affecting the propagation of the SAR signal, shows particularly strong spatio-temporal variations near the equator, while the dispersive nature of the ionosphere makes its effect stronger on low-frequencies, such as L-band signals. To tackle this problem, range split-spectrum method can be implemented to compensate the ionospheric phase contribution. Here, we apply this technique for time-series of ALOS-PALSAR data, and propose optimizations for low-coherence areas. To evaluate the efficiency of this method to retrieve subtle deformation rates in equatorial regions, we compute time-series using four ALOS-PALSAR datasets in contexts of low to medium coherence, showing slow deformation rates (mm/yr to cm/yr). The processed tracks are located in Ecuador, Trinidad and Sumatra, and feature 15 to 19 acquisitions including very high, dominating ionospheric noise, corresponding to equivalent displacements of up to 2 m. The correction method performs well and allows to reduce drastically the noise level due to ionosphere, with significant improvement compared with a simple plane fitting method. This is due to frequent highly non-linear patterns of perturbation, characterizing equatorial TEC distribution. We use semivariograms to quantify the uncertainty of the corrected time-series, highlighting its dependence on spatial distance. Thus, using ALOS-PALSAR-like archive, one can expect a detection threshold on the Line-of-Sight velocity ranging between 3 and 6 mm/yr, depending on the spatial wavelength of the signal to be observed. These values are consistent with the accuracy derived from the comparison of velocities between two tracks in their overlapping area. In the case studies that we processed, the time-series corrected from ionosphere allows to retrieve accurately fault creep and volcanic signal but it is still too noisy for retrieving tiny long-wavelength signals such as slow (mm/yr) interseismic strain accumulation.

1. Introduction

Synthetic Aperture Radar Interferometry (InSAR) is a well-established space-geodesy technique allowing to monitor a large set of geophysical phenomena, including e.g. earthquakes, volcanoes, landslides, glaciers, interseismic strain, or land subsidence (e.g. Bürgmann et al., 2000; Dzurisin, 2003). Some of them produce large and rapid ground displacements, which can be detected using simply pairs of images (interferograms), but the increasing amount of SAR data acquired by several satellites allows now to compute time-series of ground motion reaching an accuracy of a few mm/yr in the radar Line-of-Sight (LOS) (Berardino et al., 2002; Ho Tong Minh et al., 2022). However, these approaches are mostly limited by the propagation delays affecting the microwave signal when it passes through the Earth's atmosphere. A large part of this atmospheric delay is often caused by spatio-temporal variations of water vapor in the troposphere between the different acquisitions, for which compensation methods are now routinely applied (Doin et al., 2009; Jolivet et al., 2011, 2014). Yet, under some circumstances, the delay caused by spatio-temporal variations of electron content in the ionosphere can be dominating and significantly disturb the InSAR signal (Gray et al., 2000; Meyer et al., 2016).

The SAR sensors operate using different wavelengths, the most common ones being X-band (~2–4 cm, e.g. TerraSAR-X), C-band (~4–8 cm, e.g. Sentinel-1) and L-band (~15–30 cm, e.g. ALOS-PALSAR). Electromagnetic waves with large wavelength penetrate deeper through the vegetation cover, and thus are more likely to reach the

* Corresponding author.
E-mail address: leo.marconato@univ-grenoble-alpes.fr (L. Marconato).

https://doi.org/10.1016/j.srs.2023.100113
Received 8 September 2023; Received in revised form 23 November 2023; Accepted 29 November 2023
Available online 3 December 2023

stable ground, thus generally improving the general coherence. For this reason, L-band sensors are preferred for studies in equatorial regions, where dense forests are widespread and prevent the use of C or X-band sensors (e.g. Champenois et al., 2014; Morales Rivera et al., 2016; Pousse-Beltran et al., 2016; Champenois et al., 2017; Tong et al., 2018; Dianala et al., 2020). However, as ionosphere is a dispersive medium, it affects more the low-frequency (or large-wavelength) radar waves, such as the ones used by L-band sensors. Additionally, the activity of the ionosphere is mostly controlled by the intensity of incoming solar radiations, which is maximum around the equator (Kelley, 2009). Consequently, the phase advance induced by Total Electronic Content (*TEC*) which can reach several meters at equatorial regions, makes really challenging the processing of time-series of L-band SAR data (Belcher, 2008; Meyer et al., 2016). The phase patterns associated with ionosphere are often non-linear in space and cannot be satisfactorily removed by simple polynomial fitting.

Although several methods were proposed to estimate and remove ionospheric contribution from InSAR phase (Pi et al., 2011; Raucoules and de Michele, 2010; Jung et al., 2013; Li et al., 2020), the range split-spectrum method (Brcic et al., 2010; Gomba et al., 2016) was retained as the most efficient approach to correct interferograms from ionospheric noise (e.g. Liang et al., 2018, 2019). This method was extended to the compensation of time-series of InSAR data by Fattahi et al. (2017), who demonstrated its efficiency using ALOS-PALSAR data in good coherence conditions (Chile and California). This method was also extended to wide-swath acquisition modes of ALOS-2 and Sentinel-1 satellite (Liang et al., 2018, 2019), also with examples in high coherence regions. In these studies, the comparison between InSAR derived velocity maps after ionospheric correction and GNSS velocities shows an agreement reaching 2–5 mm/yr. Liao et al. (2018) adapted the split-spectrum method for InSAR measurement of ice velocity in polar regions, also prone to ionospheric disturbances, and with poor coherence conditions. However, this study only uses single interferograms (no time-series inversion), and the motions observed are rather large (several meters per year).

In this paper, we propose to evaluate the performance of the split-spectrum technique for correcting time-series of L-band InSAR data in equatorial regions. The latter are particularly challenging because (1) ionospheric perturbations are common and have strong amplitude and gradients; and (2) coherence is often low due to the dense vegetation cover, justifying the use of L-band data. We select several case studies where slow tectonic and volcanic deformations occur, and produce ground motion close to the detection limit of InSAR, such as interseismic strain on a locked fault, fault creep, and long-term volcanic inflation. In the following sections, we quickly recall the effects of ionosphere on InSAR measurement, and the theory behind the split-spectrum correction technique. Subsequently, we describe how we implemented the split-spectrum method for JAXA's ALOS-PALSAR data in the NSBAS processing chain (Doin et al., 2011), focusing on the optimizations made and aiming to the detection of small deformation rates. The selected case studies are then presented, together with their specific tectonic and volcanic contexts, as well as the previous InSAR studies carried on these areas. Then, we present the time-series derived for each case study from the ALOS-PALSAR archive, allowing us to qualitatively assess the performance of the ionospheric correction. The main geophysical signals observed in these time-series are quickly described, and compared with previous findings. Finally, we implement a quantitative assessment of the performance of the split-spectrum correction, mainly using two approaches: (1) a consistency analysis over the overlapping region between two tracks; and (2) a geostatistical analysis of the time-series' spatial variance. Throughout the study, we systematically compare the efficacy of a simple ramp fitting technique (often performed routinely in InSAR processing) with the combination of split-spectrum and ramp fitting. From this analysis, we derive an empirical accuracy of ALOS-PALSAR time-series in equatorial regions, and highlight how this accuracy depends on the distance, and thus the spatial wavelength of the considered ground deformation.

2. Methodology

2.1. Ionospheric effects on InSAR

The ionosphere is a high layer of the Earth's atmosphere, where the gases are partially ionized by solar radiations. In this region of the atmosphere, the high electronic content resulting from the photoionization can affect significantly the propagation of radio waves. In a vertical profile of the atmosphere, the higher electron densities are found between 300 and 400 km above the surface of the Earth (in the F-layer of ionosphere), because at this distance there is a balance between the increase of solar radiation energy and the decrease of gas concentration with altitude.

Electron content of the ionosphere shows spatio-temporal variations mainly controlled by the intensity of incoming solar radiations. Consequently, the Total Electron Content (*TEC*) of the ionosphere is much higher during day time than during night time, and also shows both 1-year seasonal variations and ~11-year variations related to solar cycles. Regarding the spatial distribution of TEC, high electronic concentrations are mainly located at low latitudes, where incoming solar radiations are maximum, and more specifically along two lobes located on both sides of the magnetic equator. However, several phenomena can cause TEC disturbance beyond this simple scheme (Kelley, 2009; Pi et al., 2011). At high-latitudes, ionosphere can also be perturbed by aurora activities. At middle-latitudes, the middle-latitude ionospheric trough and traveling ionospheric disturbances (TIDs) can change electronic content of the ionosphere. Finally, in equatorial regions, it was shown that plasma bubbles and ionospheric scintillation can disrupt the TEC distribution, and have important impact on SAR imagery (Belcher, 2008; Pi et al., 2011; Meyer et al., 2016).

Radio waves propagating through ionosphere undergoes three effects (Belcher, 2008): a phase advance, a group delay and a Faraday rotation, i.e. a polarimetric change. The phase advance is the main contribution of the ionosphere to interferometric SAR signal, therefore the other effects will be neglected in the following. The phase advance can be estimated approximating the ionosphere by an idealized thin layer located at the barycenter of the vertical electron density distribution. The effect of such an ionized layer on the two-way propagation of an electromagnetic wave can be derived from Appelton–Hartree equation (Belcher, 2008):

$$\varphi_{iono} = -\frac{4\pi K}{c f_0}\mathrm{TEC} \tag{1}$$

where $K = 40.28\ \mathrm{m^3/s^2}$, c is the speed of light in vacuum, f_0 is the frequency of the microwave signal, and TEC, in electrons/$\mathrm{m^3}$ is the electron content integrated along the radar signal traveling path.

Differences in TEC between two SAR acquisitions result in a phase difference mixed with other contributions in the interferometric signal. The effect of ionosphere on InSAR phase is inversely proportional to the carrier frequency of the radar signal, and thus increases with radar wavelength. Consequently, L-band sensors are more sensitive to ionospheric disturbances than C-band sensors, and X-band sensors undergo even smaller effects. For instance, the same TEC variations will create a propagation advance in meters about 16 times larger in a L-band interferogram compared to a C-band one. Using L-band sensors, such as ALOS PALSAR featuring a 23 cm wavelength, ionospheric delays reaching several meters have been observed, in particular in equatorial and auroral regions where it may become the main contribution to InSAR phase (e.g. Gomba et al., 2016; Liao et al., 2018).

A side-effect of the phase change induced by the ionosphere is the azimuth shift caused by TEC variations within the synthetic aperture view. The amplitude of this shift is proportional to the azimuth derivative of the ionospheric phase, and thus important spatial variation of

TEC can result in SAR image distortion and local decorrelation (Gray et al., 2000).

2.2. The split-spectrum method

Several approaches have been investigated in order to compensate the effect of ionosphere in InSAR phase. Among the methods developed to extract the ionospheric phase from the SAR signal itself, without using any external TEC data (e.g. from GNSS), one can differentiate approaches using Faraday rotation, azimuth shift, and range split-spectrum. Methods using Faraday rotation (e.g. Pi et al., 2011; Li et al., 2020) can retrieve absolute TEC for each acquisition, but they require full polarimetric SAR images, which are not widespread in current satellite missions. Azimuth shift based methods (e.g. Raucoules and de Michele, 2010; Jung et al., 2013) have proven to be efficient in retrieving the relative ionospheric phase screen, however they require a spatial integration, amplifying noise, and they are limited by the difficulty to separate between azimuth shifts due to ionosphere and shifts due to ground motion (for instance when studying earthquakes). Therefore, the methods based on range split-spectrum, or split-spectrum, (Brcic et al., 2010; Gomba et al., 2016) are now considered as the most reliable and accurate for the compensation of ionospheric phase in SAR interferograms. This approach consists in separating the dispersive ionospheric phase from the non-dispersive other terms of the phase difference, using two sub-bands of the range frequency spectrum.

The phase difference $\Delta\varphi$ measured by SAR interferometry can be decomposed as follows:

$$\Delta\varphi = \frac{4\pi f_0}{c}\left(\Delta r_{topo} + \Delta r_{tropo} + \Delta r_{def}\right) - \frac{4\pi K}{c f_0}\Delta\mathrm{TEC} + \varphi_{noise} \tag{2}$$

where Δr_{topo}, Δr_{tropo} and Δr_{def} are the geometric path delay, the differential tropospheric path delay, and the differential path delay associated with the ground motion between acquisitions, respectively; and φ_{noise} is the phase noise due to decorrelation. The last dispersive term corresponds to the ionospheric contribution:

$$\Delta\varphi_{disp} = \Delta\varphi_{iono} = -\frac{4\pi K}{c f_0}\Delta\mathrm{TEC} \tag{3}$$

The split-spectrum approach (Brcic et al., 2010; Gomba et al., 2016) consists in isolating $\Delta\varphi_{disp}$, the dispersive contribution from the interferogram phase, using two sub-bands cut in the radar range bandwidth. $\Delta\varphi_{iono}$ can then be estimated using two interferograms at two different frequencies f_L (left) and f_R (right):

$$\Delta\varphi_{iono} = \frac{f_L f_R}{f_0\left(f_R^2 - f_L^2\right)}\left(\Delta\varphi_L f_R - \Delta\varphi_R f_L\right) \tag{4}$$

where $\Delta\varphi_L$ is the phase of the interferogram at frequency f_L and $\Delta\varphi_R$ is the phase of the interferogram at frequency f_R. In order to obtain two interferograms focused at different frequencies, the range spectrum of the SAR image is divided into two sub-bands. To do so, the Single Look Complex (SLC) image centered at the carrier frequency f_0 is band-pass filtered in the Fourier domain, to extract two sub-band SLCs focused at f_L and f_R. Gomba et al. (2016) recommends to use non-overlapping sub-bands of one-third of the total range bandwidth, and separated by the larger possible frequency span. They also showed that the accuracy of the method is increasing with the separation between f_L and f_R, and thus with the range bandwidth.

Although quite simple in theory, the split-spectrum method implies special care for several steps in its practical implementation. *(1)* The range sub-bands extracted from the SLCs must be perfectly defined so that their central frequencies f_L and f_R are accurate. *(2)* The geometrical phase corrections of sub-bands interferograms must be computed with the corresponding frequencies. *(3)* The phase of sub-band interferograms must be unwrapped without errors prior to ionospheric phase estimation, although they are noisier than the full-band interferogram. *(4)* The combination of the sub-band interferograms extremely amplifies the interferometric noise due to the very large coefficients in Eq. (4). This very important level of noise should be compensated using efficient multilooking and filtering. Especially, the last two steps can be critical in case of low-coherence areas.

2.3. InSAR time-series processing

We use the NSBAS processing chain (Doin et al., 2011) to generate time-series of interferometric phase from ALOS-PALSAR stripmap data. First, the Copernicus GLO-30 DEM (European Space Agency, 2022), interpolated at a 15 m resolution, is used to accurately coregister the Single Look Complex (SLCs) images in a reference geometry, chosen among the acquisitions with the largest bandwidth (FBS, i.e. *Fine Beam Single polarization*). A network of interferograms (Fig. S1) is defined for each track following a Small BAseline Subset (SBAS) approach. Interferograms, corrected from geometrical path using slope-adaptive spectral shift filtering (Gatelli et al., 1994; Davidson and Bamler, 1999; Guillaso et al., 2008), are then multilooked by a factor 2 in range and 6 in azimuth (Fig. S2a). Corrections from stratified tropospheric phase delays are applied to wrapped interferograms using the ERA5 reanalysis data from the European Centre for Medium-Range Weather Forecast (ECMWF, Doin et al. 2009; Jolivet et al. 2011; Fig. S2b). Colinearity (Pinel-Puyssegur et al., 2012) is computed and replaces the amplitude of interferograms as a weighting for the subsequent multilooking step, which leads to final factors of 8 in range and 24 in azimuth. Interferograms are then filtered using a sliding window weighted by the multilooked colinearity. Finally, filtered interferograms are unwrapped using a region-growing algorithm that expands the unwrapping from high to low colinearity areas (Doin et al., 2023), and the unwrapped interferograms are carefully checked by hand (Fig. S2c). Phase ramps in range and in azimuth are estimated on each interferogram, and the phase ramps network is inverted to retrieve the phase ramp per image (Biggs et al., 2007). The latter is used to flatten the interferograms or not, depending on the purpose for performance assessment as described in the following sections. Eventually, the phase of all interferograms is referenced prior to the time-series inversion by subtracting the average phase of an area containing *a priori* no deformation signal.

The unwrapped interferograms are then inverted in time-series following the approach of López-Quiroz et al. (2009), Doin et al. (2011) and Ho Tong Minh et al. (2022). We obtain a data cube containing the relative phase for each SAR acquisition. For plotting, we systematically referenced the phase maps with respect to the average of the acquisitions including the least ionospheric noise, in order to get a distributed reference over the time-series. The Root Mean Square of the network phase misclosure (hereafter referred as RMS misclosure; López-Quiroz et al., 2009) is used to mask the time-series maps. We also derive a velocity map from the time-series by iteratively (1) fitting it by a linear function of time and (2) down-weighting the acquisitions with large residuals.

2.4. Implementation of the split-spectrum correction

The implementation of the split-spectrum method that we used to correct time-series from ionospheric phase is displayed on a flowchart in Fig. S3, and specific features are explained hereafter.

1. *Sub-bands separation:* The first step of the split-spectrum method consists in generating sub-band SLCs from the initial full-band SLCs, before their coregistration. The range spectrum is first normalized between $f_0 - B'/2$ and $f_0 + B'/2$, where B' is set to 95% of the effective bandwidth B, discarding the highest frequencies of the SLC. The spectrum is indeed tapered to zero during the SLC focusing by a sinus cardinal convolution. The null part of the spectrum is due to oversampling with respect to the actual image range resolution.

Normalization then ensures that the barycentre of the spectrum is consistent between both reference and secondary images, and between the two sub-band SLCs. As ALOS-PALSAR operated in both single-polarization (FBS) and dual-polarization (FBD) modes, the theoretical effective bandwidth can vary from one acquisition to another (between 28 and 14 MHz, respectively). We limit systematically the spectrum using $B = 14$ MHz for sub-band calculation, except for pairs involving two FBS acquisitions, in which case we use $B = 28$ MHz. A band-pass filter, spanning 1/3 of $B^{'}$ is then applied to the range spectrum. The resulting sub-bands are finally shifted from their central frequencies to be centered at zero before inverse FFT.

2. *Sub-band interferograms generation:* The next step consists in generating the sub-band interferograms by combining the sub-band SLCs. Prior to interferogram generation, the sub-band SLCs are coregistered using the offsets previously computed for the full-band SLCs. Then, interferograms are generated, taking into account the new central frequencies of the sub-bands to compute and compensate the geometric phase $\Delta\varphi_{topo}$. They are then multilooked to reach multilooking factors of 8 in range and 24 in azimuth, using colinearity computed for each sub-band interferogram as a weight, just as full-band interferograms. The amplitude of the multilooked interferogram, noted $C^{L/R}_{8rlks}$, is a measure of the interferogram coherence.
3. *Phase unwrapping:* This is a critical step as phase unwrapping errors will be highly amplified in the combination used to estimate non-dispersive phase (Eq. (4)), especially if they are not common between the two sub-band interferograms (Gomba et al., 2016). It is even more critical because the sub-band interferograms are noisier compared to the full-band ones because of their smaller frequency content. To get around this problem, in our implementation, the carefully unwrapped full-band filtered interferogram $\varphi^{full-band}_{filt,unw}$, obtained in Section 2.3, is used to unwrap the sub-band ones in two steps. First, we compute the unfiltered unwrapped interferogram $\varphi^{full-band}_{unw}$, by adding its missing high-frequency content, according to:

$$\varphi^{full-band}_{unw} = \varphi^{full-band}_{filt,unw} + arg_{[-\pi,\pi]}\left[e^{j\left(\varphi^{full-band}_{wrap} - \varphi^{full-band}_{filt,wrap}\right)}\right] \quad (5)$$

where the right term is the wrapped phase difference between the filtered and the non-filtered interferograms. As the full-band unfiltered interferogram and the sub-band interferograms contain the same information, except for a small fraction of the ionospheric phase term and the noise, which we assume included in $[-\pi,\pi]$, we can use:

$$\varphi^{L/R}_{unw} = \varphi^{full-band}_{unw} + arg_{[-\pi,\pi]}\left[e^{j\left(\varphi^{L/R}_{wrap} - \varphi^{full-band}_{unw} - \overline{\varphi}^{L/R}_{res}\right)}\right] \quad (6)$$

where $\varphi^{L/R}_{wrap}$ is the phase of the wrapped sub-band interferogram and $e^{\overline{\varphi}^{L/R}_{res}}$ the spatial average over the whole interferogram of the complex residue $e^{j\left(\varphi^{L/R}_{wrap} - \varphi^{full-band}_{unw}\right)}$. The latter is subtracted in order to ensure that the phase residual between the full-band and sub-band interferograms is centered on zero.

4. *Weighted multilooking:* Fortunately, the ionosphere is usually rather smooth and thus the dispersive phase delay is spatially correlated. This enables the use of spatial filtering in order to increase the accuracy of the ionosphere phase estimate (Gomba et al., 2016). We replace the amplitude of sub-band interferograms by a weight which will be used to increase the accuracy of subsequent multilooking and filtering steps. This weight, $W^{L/R}_{8rlks}$, quantifying the reliability of each pixel, is built with the colinearity $C^{L/R}_{8rlks}$, defined in step 2, and the phase residual from the unwrapping step $\varphi^{L/R}_{res} = arg_{[-\pi,\pi]}\left[e^{j\left(\varphi^{L/R}_{wrap} - \varphi^{full-band}_{unw} - \overline{\varphi}^{L/R}_{res}\right)}\right]$:

$$W^{L/R}_{8rlks} = C^{L/R}_{8rlks}.exp\left(-\frac{\varphi^{L/R^2}_{res}}{\sigma^2_W}\right) \quad (7)$$

where the σ_W parameter is the standard deviation of a gaussian function, and should be adapted depending on the observed level of noise. According to Eq. (7), the weight of pixels for which the phase residual is close to 0 will remain high, but it will be reduced for pixels with high phase residual (i.e. inconsistent between full-band and sub-band interferograms). Using this weight, starting from sub-band interferograms with multilooking of 8 in range and 24 in azimuth, we apply further multilooking to reach 32 in range and 96 in azimuth. The resulting pixel spacing is about 200 m. The amplitude of multilooked interferograms is then noted $W^{L/R}_{32rlks}$.

5. *Combination, filtering and interpolation:* Then, the sub-band interferograms are combined following Eq. (4), to produce a raw estimate of the ionospheric phase screen (hereafter IPS, Fig. S2e), associated with a weight $W^{iono}_{32rlks} = W^{L}_{32rlks} \times W^{R}_{32rlks}$, which reflects the confidence we have in each pixel of the IPS. For filtering, we follow the iterative approach recommended by Fattahi et al. (2017). This consists in masking low coherence areas, using a threshold W^{iono}_{min}. Then, the masked areas are filled through nearest-neighbor interpolation, and the result is low-pass filtered. During the next iterations, the valid areas ($W^{iono}_{32rlks} > W^{iono}_{min}$) are reset to their unfiltered values, while the masked region are filled by interpolating the filtered data, before the next filtering step. The low-pass filter used is a 2D Gaussian filter with a standard deviation of 50 pixels. Phase gradient is computed and removed in a 150 pixels sliding window prior to filtering and reintroduced afterwards, and W^{iono}_{32rlks} is used as a weighting. This approach allows to get a smoothed map of the ionosphere phase delay estimated by the split-spectrum method, extrapolated in areas with very low coherence (Fig. S2e).
6. *Time-series inversion:* Following Fattahi et al. (2017), we extend the split-spectrum technique to time-series analysis by inverting the connected network of IPS to get an ionospheric delay map for each date. This approach aims to get consistent ionospheric corrections through the network, and to reduce the noise by exploiting the redundancy of ionospheric estimations in the interferometric network. As the noise increases with perpendicular and temporal baselines, we apply for the inversion a *temporal* weight inversely proportional to these two terms. This allows a better fit of short baselines ionospheric maps. A complementary *spatial* weighting is implemented using the filtered weight map W^{iono}_{32rlks}, aiming to underweight low-coherence areas. The weight of each data point in the inversion is thus equal to the product of the *temporal* weight and the *spatial* weight.

The resulting time-series of IPS is used to compute improved pairwise corrections by recombining the acquisitions according to the SBAS network (Fig. S2f). These new corrections are interpolated to match the resolution of full-band interferograms, from which they are then subtracted (Fig. S2g). The end of the processing is done as described in Section 2.3, resulting in a time-series of interferometric phase corrected from ionospheric perturbations.

2.5. Measurement of the time-series' accuracy

To evaluate the performances of the ionospheric correction on the final time-series of interferometric phase, we mainly use the statistical spatial dispersion of the phase at each time step. As the ionospheric noise is dominating in the datasets presented hereafter, we assume that the dispersion reflects mostly this contribution, and is thus a good indicator of the quality of the correction. The output of the time-series inversion is

obtained relative to the first period, which residual atmospheric contribution contaminates all successive maps. To avoid this, we subsequently compute the average of the 3 to 6 acquisitions containing the least ionospheric noise, i.e. the images with the lower variances before ionospheric correction and use this map to reference de time-series. Then, to investigate the spatial variability of phase dispersion, we compute semivariograms at each time-step, using a sub-sample of 5000 pixels covering the whole spatial extent, and compute the square root of the semivariance, called hereafter σ, in radians or meters. In order to target the characteristic spatial roughness of ionospheric patterns (about tens of kilometers), we extract from variograms σ at a specific 50 km distance, and call it σ_{50}. Illustration of the applications of those metrics will be given in the following sections.

3. Case studies

Three areas were chosen to evaluate the ionospheric correction implemented in this study: Ecuador, Trinidad and Sumatra. They are all located in equatorial regions, at latitudes within 11° from the geographic equator, where the TEC variations and disturbances are the most important. Moreover, at these latitudes, the land is mostly covered by a dense vegetation, which make the use of L-band sensors relevant. These areas are thus good case studies for assessing the performance of the ionospheric correction in slow deformation contexts.

3.1. Ecuador

Ecuador is located along the South American subduction zone, where the Nazca plate plunges under the South-American continent (Fig. 1a). There, the obliquity of the convergence results in partitioning between the subduction megathrust and a major strike-slip fault system. The latter, called Cosanga-Chingual-Pallatanga-Puna (CCPP), limits a continental sliver (Alvarado et al., 2016, Fig. 1a). GNSS studies has shown that this fault system accommodates 0.5–1 cm/yr of right-lateral deformation (Nocquet et al., 2014), yet this motion has never been clearly observed by InSAR. This is probably due to the dense vegetation in the lowlands, important topography gradients in the Andean cordilleras, and large ionospheric noise. On the other hand, the subduction causes a significant volcanic activity in Ecuador, with about nine volcanoes active currently. Among them, Tungurahua (Fig. 1a) is an andesitic stratovolcano with intermittent activity since 1999, which last erupted in 2006. Large-scale inflation was observed on this volcano using InSAR time-series of Envisat (Champenois et al., 2014) and ALOS-PALSAR (Morales Rivera et al., 2016) data. However, these studies do not include a procedure for compensating ionosphere noise. For instance, Morales Rivera et al. (2016) indicate that they eliminated the ALOS acquisitions contaminated by important ionospheric signals, i.e. 17% of their dataset.

We process two ascending tracks of ALOS-PALSAR data over southern Ecuador, using five frames for each track, resulting in the coverage of ~150 × 400 km region (Fig. 1a). This region encompasses the CCPP and the Tungurahua volcano. Both tracks include 18 complete acquisitions between late-2006 and early-2011 (Table 1).

Table 1
Information about ALOS-PALSAR data used for the different case studies.

	Track	Frames	First acquisition	Last acquisition	Number of acquisitions
Ecuador dataset	T110	7120–7160	2006/12/23	2011/01/03	18
	T111	7130–7170	2007/01/09	2011/03/07	18
Trinidad dataset	T119	0190–0200	2007/01/07	2011/03/05	19
Sumatra dataset	T499	0080	2007/01/27	2010/11/07	15

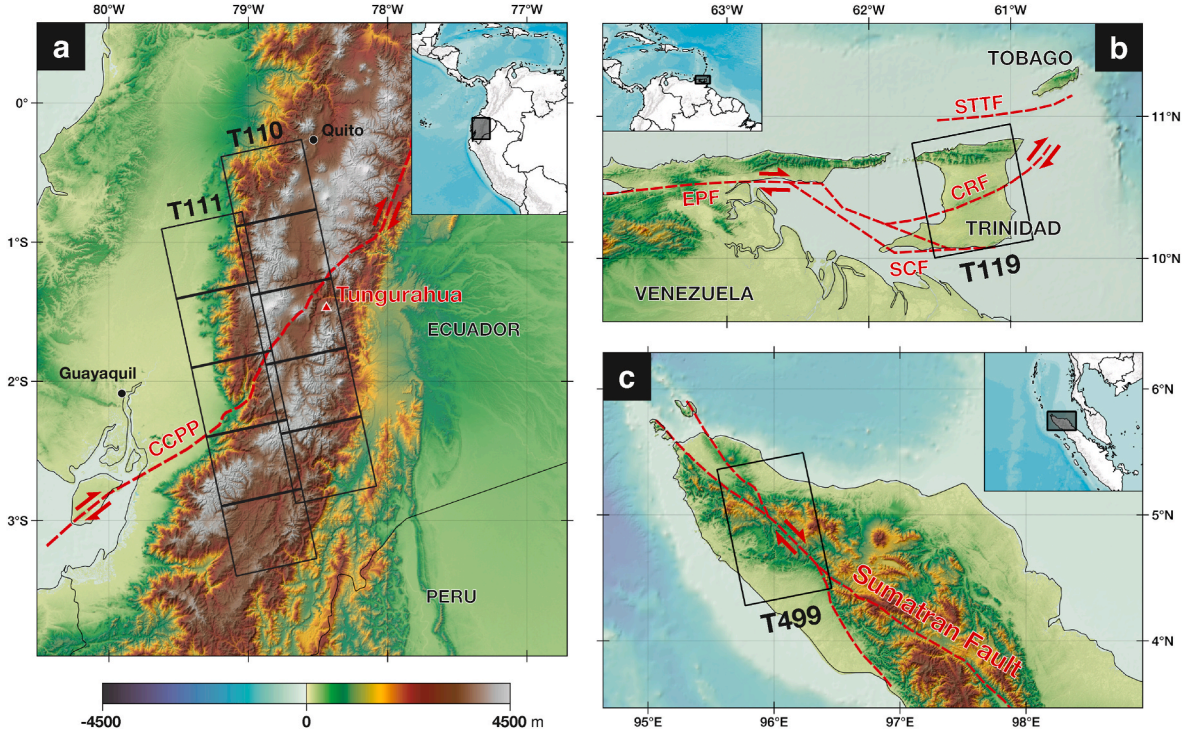

Fig. 1. Tectonic (and volcanic) contexts of the 3 case studies. Black outlines mark the footprints of ALOS-PALSAR acquisitions used in this study. Major faults are shown with red dashed lines. (a) Ecuador case study. Tungurahua volcano is indicated by the red triangle. CCPP: Cosanga-Chingual-Pallatanga-Puna Fault system. (b) Trinidad case study. EPF: El Pilar Fault; STTF: Sub-Tobago Terrane Fault; CRF: Central Range Fault; SCF: South Coast Fault. (c) Sumatra case study. Copernicus GLO-30 and GLO-90 data are used for topography, SRTM15+ data is used for bathymetry. (For interpretation of the references to color in this figure legend, the reader is referred to the Web version of this article.)

3.2. Trinidad

Trinidad-Tobago is located in the northern part of South-America (Fig. 1b), on the Caribbean-South American transform plate boundary that accommodates about 2 cm/yr of right-lateral motion between the two tectonic plates (Weber et al., 2001). In particular, fault creep has been observed on the El Pilar Fault (EPF, Fig. 1b), west of Trinidad-Tobago, using GNSS (Jouanne et al., 2011) and InSAR (Pousse-Beltran et al., 2016). The Trinidad island itself is structured by several main faults, including the Sub-Tobago Terrane Fault (STTF), the South Coast Fault (SCF) and the Central Range Fault (CRF) (Fig. 1b). Higgins et al. (2021) showed using both GNSS and ALOS-2 InSAR time-series that the CRF and SCF are creeping at a 14.5 mm/yr and 3 mm/yr rates, respectively.

We processed an ALOS-PALSAR ascending track over southern Trinidad, using two frames covering most of the island, including the CRF (Fig. 1b). The dataset includes 19 complete acquisitions between early-2007 and early-2011 (Table 1).

3.3. Sumatra

Sumatra is located along a subduction zone where the Indo-Australia plate plunges under the Sunda microplate. There, oblique subduction leads to right-lateral motion on the Sumatran Fault (Fig. 1c) located in the forearc region. Although the Sumatran fault is almost 2000 km long, we focus on its northernmost part, in the Aceh segment, where fault creep at a rate of 1.6–2.0 cm/yr was first observed using GNSS between 2005 and 2010 (Ito et al., 2012). Tong et al. (2018) found consistent results using time-series of ALOS-PALSAR data. Their study used no ionospheric compensation procedure, and rejected the contaminated interferograms.

We processed one frame of an ALOS-PALSAR ascending track crossing the northernmost part of the Sumatran fault (Fig. 1c). The dataset includes 15 acquisitions between early-2007 and late-2010 (Table 1).

4. Results

Using the InSAR processing workflow defined in Section 2, we computed time-series for each of the four selected tracks using different correction strategies: first without any correction, second with phase ramp removal, third with ionospheric phase screen removal (IPS, from time-series-improved split-spectrum procedure described in Section 2.4) and finally combining the IPS and ramp removal.

4.1. Ecuador

Fig. 2a shows an example of time-series for track 110 without any correction related to ionosphere, hereafter referred as *raw time-series*, as the only corrections applied are a geometric phase correction and a stratified delay compensation using ERA5 model. Each acquisition is masked for RMS misclosure higher than 0.6 rad. Interestingly, significant ionospheric noise is observed in most acquisitions of this track, corresponding to delays ranging between between 30 cm and 2 m. As among the four tracks we processed, track 110 is the one displaying the largest ionospheric noise, with a wide diversity of patterns, we will use it as main example. One can indeed note on Fig. 2 that the ionospheric patterns vary a lot, from almost linear ramps (e.g. 20070625 or 20100703) to highly non-linear patterns, characterized by large anisotropic phase gradients (e.g. 20080627 or 20090825).

As a consequence of this frequent non-linear behavior of ionospheric noise, ramp fitting and removal, which is often routinely applied in InSAR processing chains, appear largely insufficient for correcting it (Fig. 2b). First, the acquisitions containing *a priori* linear patterns display non negligible residuals as the actual ionospheric delays are in most of the cases slightly convex or concave (e.g. 20080327, with about 25 cm of residual delay after ramp removal). Also, the acquisitions containing highly non-linear patterns show very limited improvement, as for example for acquisition 20080627, for which the variogram still show a plateau around 8 radians (~15 cm) for distances larger than 50 km, after the ramp removal. This example illustrates the need of a more sophisticated method of ionospheric phase compensation for processing L-band data over equatorial areas.

By contrast, the split-spectrum correction appears to compensate most of the ionospheric noise, including most of large azimuth and range ramps (e.g. 20080327, Fig. 2c). This Ionospheric Phase Screen also corrects very well the highly non-linear patterns (e.g. 20080627 or 20101003). Some residual ramps are still visible on the IPS corrected maps, whose amplitude is small and whose sign is not always the same as the one of the initial ionospheric gradient (e.g. 20080327 or 20080812). Therefore, part of these residual ramps could also originate from orbital errors.

Finally, one can notice on Fig. 2d that after the complete correction (IPS + ramps), most acquisitions are brought to a much more homogeneous level of dispersion (confined below ~5 cm, Fig. 3a). Some artifacts are still present in a small number of acquisition (e.g. in 20080627, 20090815 or 20110103) due very large phase gradients in range, that cannot be retrieved by the low-pass filtered IPS. However, the amplitude of these has been reduced drastically by the correction, and their impact on the velocity fitted in the time-series is now negligible (Fig. 2d, last column).

The IPS maps are shown on Fig. 2e. They are computed from time-series inversion of the products of the split-spectrum method applied to each interferogram. The RMS misclosure of this IPS time-series (Fig.. 2h and 3b) describes the average residual between estimated and reconstructed pairwise IPS constraining a given acquisition. High RMS misclosure indicated large discrepancies between the different corrections associated with one acquisition in the network. The RMS misclosure value are large, of the order of 6 cm. This discrepancy between redundant measurements quantifies the error made on individual IPS estimation. RMS misclosure correlates at first order with the improvement brought by the time-series inversion of the ionospheric correction on the displacement time-series (solid versus dashed red lines in Fig. 3a). This shows that time-series inversion of ionospheric correction is always valuable (it never worsens the correction), but has more effect on acquisitions that are very perturbed by the ionosphere (high σ in Fig. 3a).

Yet, even after the time-series inversion, the IPS still present artifacts on the lower-left and upper-right corners of the images, with abnormal patterns with respect to the rest of the IPS. These areas are also characterized by large IPS network misclosure (Fig. 2h). They correspond to very low interferometric coherence regions (below 0.2) owing to the dense tropical vegetation in the lowlands. The masking-interpolation-filtering procedure is not sufficient to avoid artifacts in these regions, because of the large noise amplification caused by the split-spectrum combination. Nevertheless, even classical InSAR time-series are being masked out due to noise in such low-coherence areas. We thus argue that the ionospheric correction implemented in this study allows to correct efficiently time-series where interferometric coherence allows the data to be used.

The same conclusions can be drawn from the analysis of track 111 (Fig. S4). In particular, one acquisition (20080112) displays an extreme ionospheric gradient in the range direction (up to 8 fringes within the image width), which is dramatically reduced by the correction, but still shows important residuals due to the limit of the method to retrieve very fine gradient fluctuations.

Using time-series corrected from split-spectrum and phase ramps for both tracks 110 and 111, we produce a consistent velocity map covering the southern part of the Ecuadorian cordilleras (Fig. 4a). Note that the RMS misclosure corresponding the time-series inversion of the corrected interferograms stays below 1 radian (Fig. 3b), indicating the absence of large unwrapping errors. Although the 2010 Pisayambo earthquake (Champenois et al., 2017), which occurred on a strand of the CCPP fault

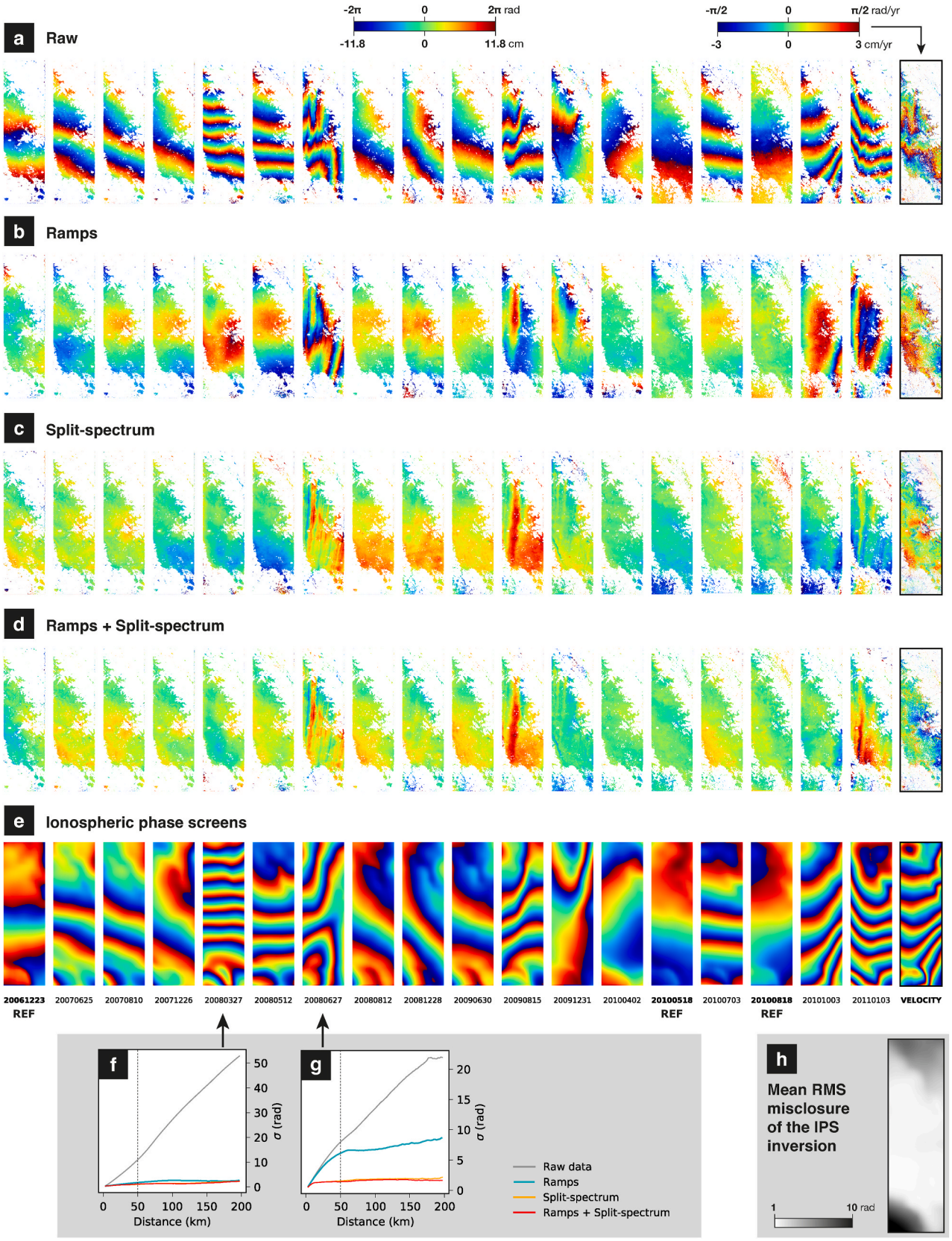

Fig. 2. InSAR time-series for ALOS-PALSAR track 110, in radar geometry. The maps show LOS phase delays relative to the average of the less noisy acquisitions marked with a REF tag (see text for details). The last image of each row shows the LOS velocity map obtained by linear fitting of the time-series. Negative velocity indicates displacement toward satellite. Each acquisition is masked where the RMS misclosure per acquisition is higher than 0.6 rad. (a) Raw time-series without any correction related to ionosphere; (b) time-series after removal of a phase ramp only; (c) time-series after removal of the IPS from split-spectrum correction only; (d) time-series after removal of both a phase ramp and the IPS, the latter are shown in (e). (f, g) Examples of variograms for the acquisitions 20080327 and 20080627, for different correction ionospheric correction strategies. (h) Map of mean RMS misclosure for the inversion of IPS: black areas correlate with low coherence areas.

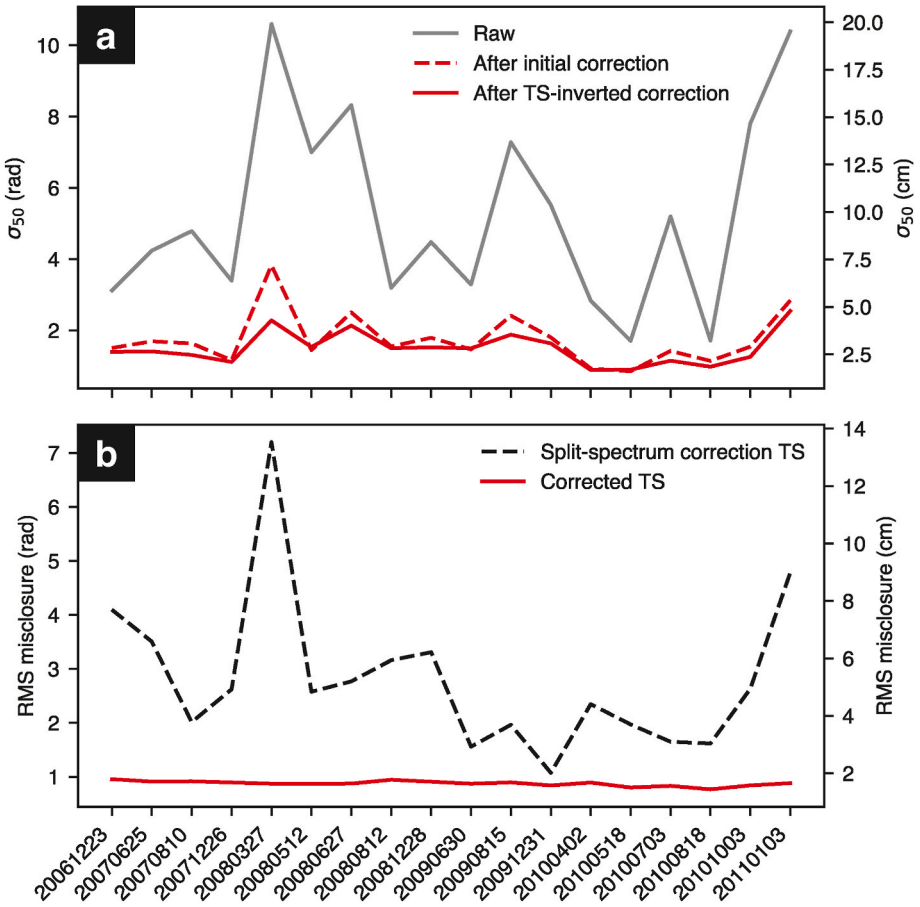

Fig. 3. (a) Square-root of semi-variogram at a 50 km distance (σ_{50}) for each acquisition of track 110. Values for the raw time-series are shown by the grey line; values for the time-series corrected using direct products of the split-spectrum method are shown by the dashed red line; and values for the time-series corrected using the products of the IPS time-series are shown by the solid red line. (b) Mean RMS misclosure for each acquisition of the track 110: network misclosure for the IPS time-series (dashed black line) and network misclosure for the time-series of InSAR data after ionospheric correction (red line). (For interpretation of the references to color in this figure legend, the reader is referred to the Web version of this article.)

system, is visible on the velocity map, our results show no hint of interseismic deformation along this fault system. Nevertheless, the velocity map shows one main deformation pattern around the Tungurahua volcano, characterized by a large-scale (~25 km around the summit) inflation, previously observed by Champenois et al. (2014) and Morales Rivera et al. (2016). The mean LOS velocity exceeds 3 cm/yr toward the satellite near the summit, in the western flank of the volcano.

Improvements brought by the ionospheric correction are also very clear on time-series of LOS displacement. Three permanent GNSS stations located on track T110 were acquiring data during the ALOS period, and could be used as benchmarks (Blewitt et al., 2018; Fig. S8). The error on the estimation of relative LOS velocities between 2 stations separated by 28 km is reduced by our correction from 1.6 cm/yr (raw time-series) to 0.4 cm/yr (fully corrected time-series) (Figs. S8a and d). For 2 station separated by 113 km, it is reduced from 12 cm/yr to 1 cm/yr (Figs. S8b and e). Likewise, in Fig. 5a, we compare the time-series of LOS deformation on the volcano relative to a nearby point, obtained without correction, after ramp removal and after full ionospheric correction. It can be seen that the main effect of the ionospheric correction is to compensate the acquisitions affected by large ionospheric disturbance appearing as outliers in the time-series. For instance, the RMSE of the linear regression to this data is reduced from 8.5 cm in the raw time-series to 2.4 cm in the fully corrected one. Interestingly, the corrected time-series displays a clear transient phase of increased inflation rate between 2008.0 and 2008.5, which cannot not be resolved without the split-spectrum correction. Another, less clear, period of increased inflation rate is in 2010. This change is synchronous to a period of increased explosion and seismicity rates (Global Volcanism Program, 2013).

4.2. Trinidad

Time-series of displacement before and after ramp and ionospheric corrections together with IPS time-series are displayed in Fig. S5. The amplitude of IPS in Trinidad is lower than that in Ecuador, probably because it is further away from geomagnetic equator. Most acquisitions show ionospheric phase changes <10 cm, but 7 acquisitions (out of 19) display significant ionospheric contamination (>25 cm). Among them, 4 acquisitions show mostly linear patterns, almost entirely corrected by ramp fitting, and 3 are characterized by very rough patterns, resulting in large residuals after the ramp removal.

The split-spectrum correction allows to significantly reduce these residuals and homogenize the dispersion of the acquisitions as, after the correction, σ_{50} is homogeneously reduced below 7 cm. However, in some acquisitions, residuals are higher than for the Ecuador tracks. This occurs because the mean interferometric coherence is low over Trinidad (around 0.2). Corrections are thus noisier in Trinidad, preventing the recovery of some steep phase gradients due to ionosphere. Consequently, the velocity map resulting from the corrected time-series is still affected by residual ionospheric noise (Fig. 4b). Nevertheless, a well-defined creeping signal is visible on the Central Range Fault, and is particularly clear on the western part of the island, where coherence is higher. The relative deformation through time of two points on each side of the creeping fault (Fig. 5b) shows the significant improvement

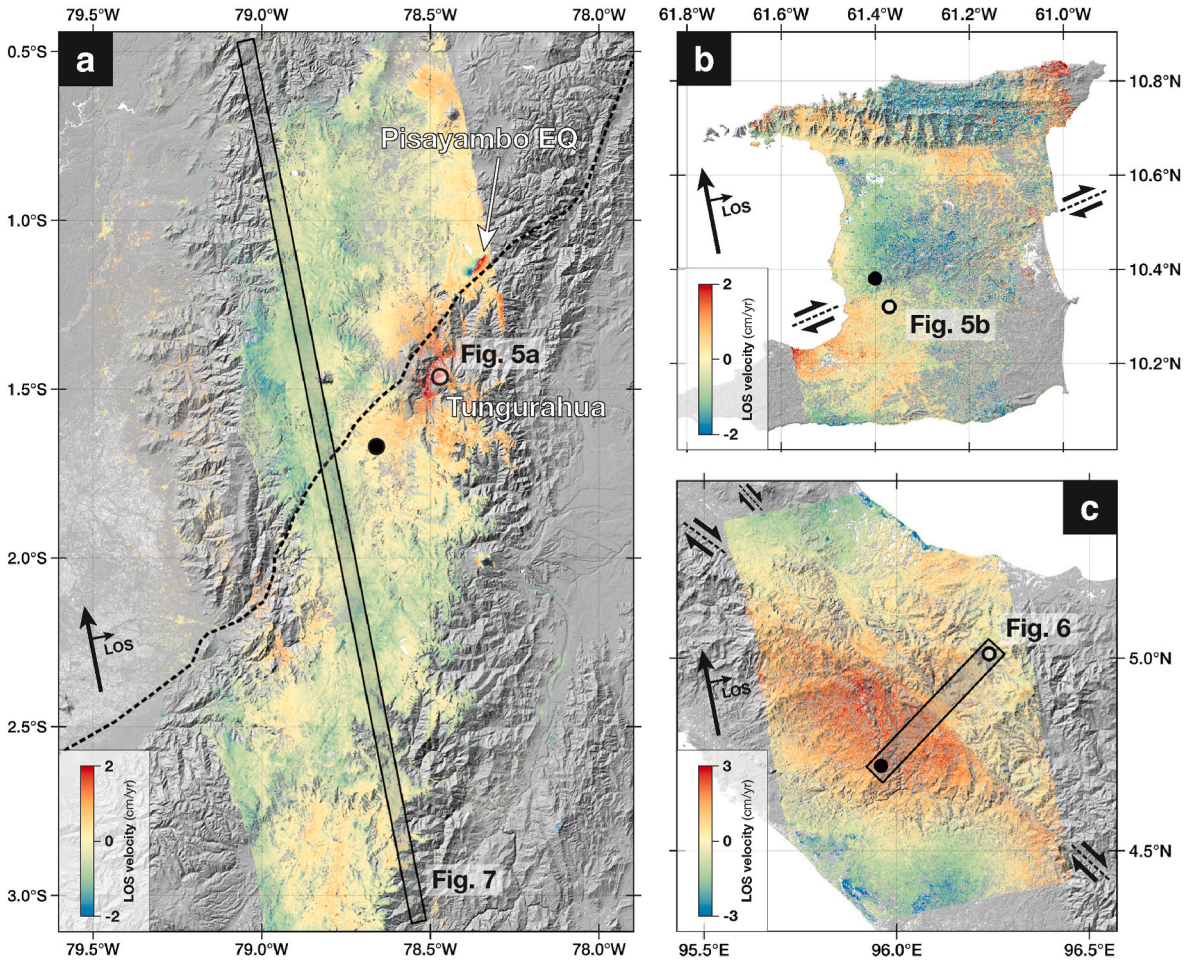

Fig. 4. Geocoded LOS velocity maps obtained after split-spectrum and ramp correction, with localization of the data used in the next figures. Positive velocity indicates displacement toward satellite. (a) Ecuador case study. The CCPP fault system is shown by the dashed line. The black rectangle indicates the profile in the track overlap area shown in Fig. 7. (b) Trinidad case study. (c) Sumatra case study. The black rectangle indicates the profile across the Sumatran Fault shown in Fig. 6. The empty circles indicate the location of the time-series of LOS displacement shown in Fig.. 5 and 6d, with the solid circles as reference point. Copernicus GLO-30 and GLO-90 data are used for topography. The reader is referred to Fig. S7 for velocity maps without ionospheric compensation.

brought by the ionospheric correction procedure. The RMSE of a linear fit to this data is reduced from 2.0 cm in the raw time-series to 0.9 cm in the fully corrected one. Note that the first acquisition of the time-series remains an outlier after the correction, which may be due to the effect of DEM errors accentuated by its very large perpendicular baseline (>2000 m). Aside from two outliers, the linear trend is now very well defined after correction, implying a constant creep rate during the 2007.5–2011 time-span.

4.3. Sumatra

The InSAR and IPS time-series for track 499 are shown in Fig. S6. The amplitude and shape of IPS in Sumatra are similar to the ones in Trinidad. More than two thirds of the acquisitions (11 out of 15) show limited ionospheric noise, satisfactorily corrected by ramp fitting. However, the perturbed acquisitions display very rough patterns, which can be mostly compensated by the split-spectrum correction, but not totally suppressed. Indeed, the coherence over this area is even worse than in Trinidad (mean coherence around 0.15), making more difficult the recovery of ionospheric phase from split-spectrum technique. However, the velocity map obtained from the corrected time-series shows a clear creeping signal on the Sumatran Fault, consistent with the findings of Tong et al. (2018). Profiles across the Sumatran fault drawn at each time step (Fig. 6) show the dramatic improvement brought by the ionospheric correction. The northeastern part of the profiles is better sorted according to time in the corrected time-series while it is very messy prior to the correction. Moreover, profiles appear to be flattened on both sides of the fault after the correction, showing that this procedure helps to stabilize the far field deformation field in the case of fault studies (Fig. 6c). This is confirmed by looking at relative time-series of displacement between points at ~20 km from the fault (Fig. 6d). Yet, the profiles are not totally flattened after our correction, and the time-series still contains important noise, which is strongly correlated to the perpendicular baseline of acquisitions (Fig. 6e). This indicates that the largest source of error remaining in this example after the ionospheric correction is DEM errors, whose effect is amplified by the large perpendicular baselines (sometimes larger than 1000 m) in ALOS-PALSAR acquisitions. DEM error correction could be performed to reduce this noise, following for instance the procedure of Ducret et al. (2014), but is beyond the scope of this paper.

5. Performance of the split-spectrum correction

To assess quantitatively the performance of the split-spectrum correction, we use two approaches. First, we take advantage of the overlap between two tracks in our Ecuadorian dataset to carry out a consistency analysis. Second, by analyzing systematically the statistical dispersion of our time-series, we evaluate the noise level remaining once the ionospheric compensation procedure has been applied.

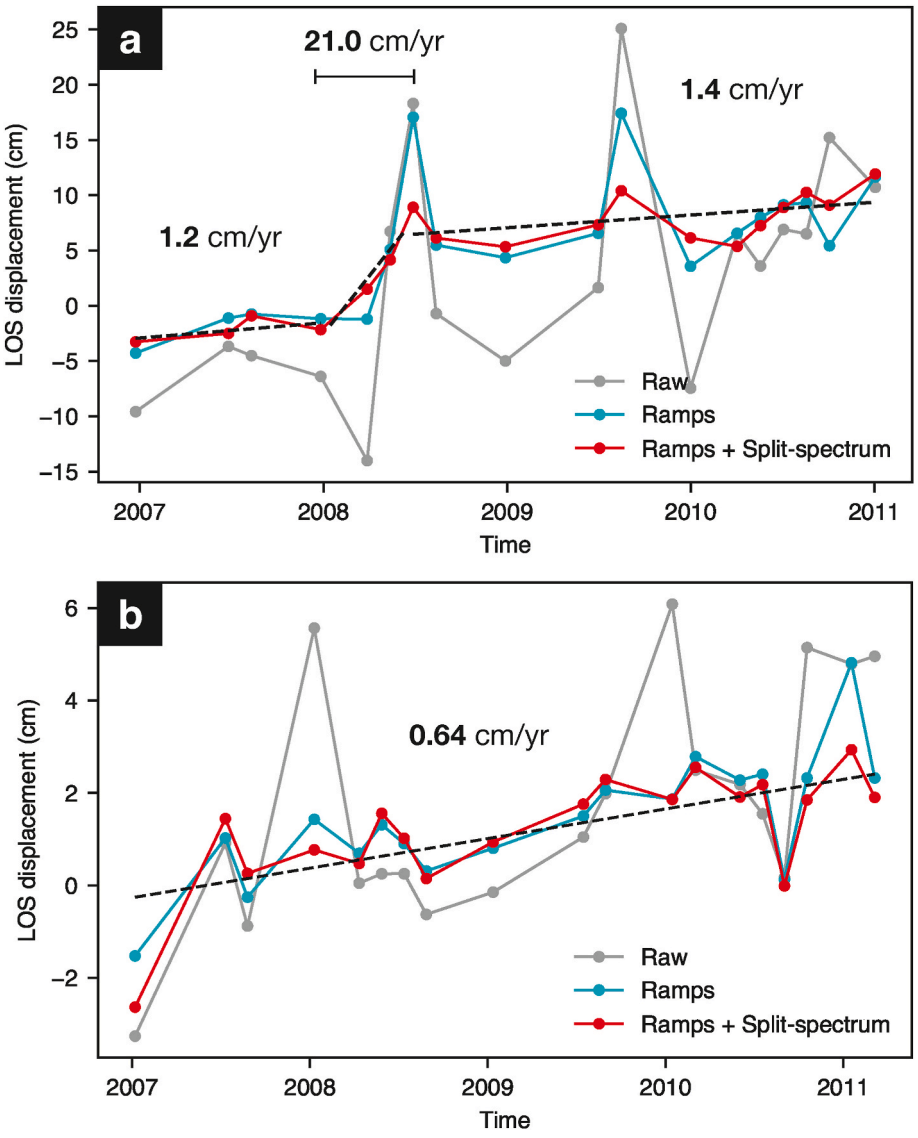

Fig. 5. Relative time-series of LOS displacement showing (a) inflation at Tungurahua volcano and (b) fault creep at Central Range Fault in Trinidad. See Fig. 4 for the locations of time-series sampling and reference points. Positive velocity indicates displacement toward satellite. In grey: raw time-series; in blue: time-series after removal of a phase ramp only; in red: time-series after the split-spectrum correction and after removal of a phase ramp. Dashed black lines show linear velocities fitted in the fully corrected time-series, with the associated rate in black. (For interpretation of the references to color in this figure legend, the reader is referred to the Web version of this article.)

5.1. Accuracy across overlapping areas

The two adjacent tracks T110 and T111 in Ecuador, include a 15 by 300 km^2 overlapping region (Fig. 1). We thus extract an along-track profile of mean velocity in this area, for both T110 and T111, for different correction strategies. The profiles of LOS velocity from raw time-series (Fig. 7a) show the same general trend, with a velocity variation of ~6 cm/yr along the profile. The same LOS velocity profiles extracted from the time-series corrected by removing ramps (Fig. 7b) still show strong velocity variations (2–4 cm/yr), inconsistent between both tracks and unrelated to plausible tectonic motions in Ecuador. Finally, the LOS velocity profiles from the time-series corrected by both split-spectrum and ramp removal (Fig. 7c) show a flattened velocity distribution, down to the ±1 cm/yr interval. This shows the efficiency of the split-spectrum compensation approach and moreover suggests that residual ramps are better estimated on interferograms once they are corrected of the IPS. The residual LOS velocity fluctuations, higher for track 111 than for track 110, likely stem from residual atmospheric delays and DEM errors, as part of them seem to correlate with the topography.

We analyze quantitatively the consistency of the profiles from Fig. 7b and c in Fig. 8. Two subsets, separated by a 1.2 rad threshold on RMS misclosure, are created in order to differentiate low and high coherence areas (corresponding to high and low RMS misclosure, respectively). Regarding the low RMS misclosure dataset, the LOS velocity with ramp removal only (Fig. 8a) seems linearly correlated between the two tracks. However, this correlation diverges from the one-to-one relationship, with larger velocities for the track 111, especially for distances along the profile ranging between −50 and 150 km. This indicates a strong spatially correlated noise, due to uncorrected ionospheric contribution. After the split-spectrum correction (Fig. 8b), the dispersion is significantly reduced, as the RMS of the velocity difference between the two tracks is reduced from 1.36 to 0.31 cm/yr. Also, the distribution of the differences is centered on zero and has a gaussian shape, which was not

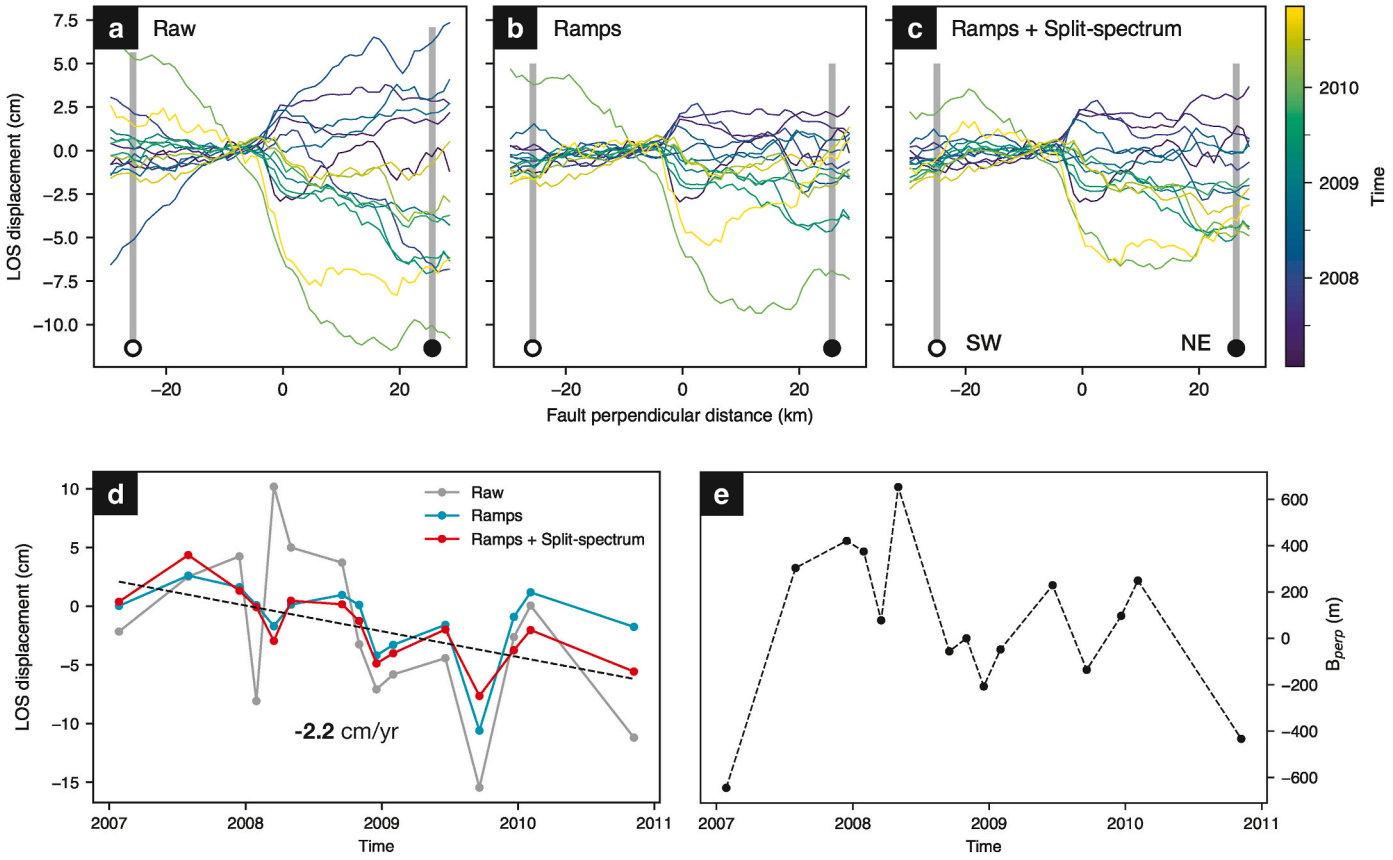

Fig. 6. Profiles of LOS displacement across the Sumatran fault, color-coded according to time. See Fig. 4 for the location of the profile. Positive values indicate displacement toward satellite. All profiles are referenced by subtracting the mean value at distances between −15 and −2 km from the fault on its SW side. (a) Raw time-series; (b) time-series after removal of a phase ramp only; (c) time-series after the split-spectrum correction and after removal of a phase ramp. (d) Relative time-series of LOS displacement between the white and black points shown on the profiles and on Fig. 4, showing far-field deformation across the Sumatran fault. See caption of Fig. 5 for details. The fully corrected time-series is strongly correlated to the perpendicular baseline of shown in (e), indicating that after ionospheric correction, the main sources of noise are DEM errors. (For interpretation of the references to color in this figure legend, the reader is referred to the Web version of this article.)

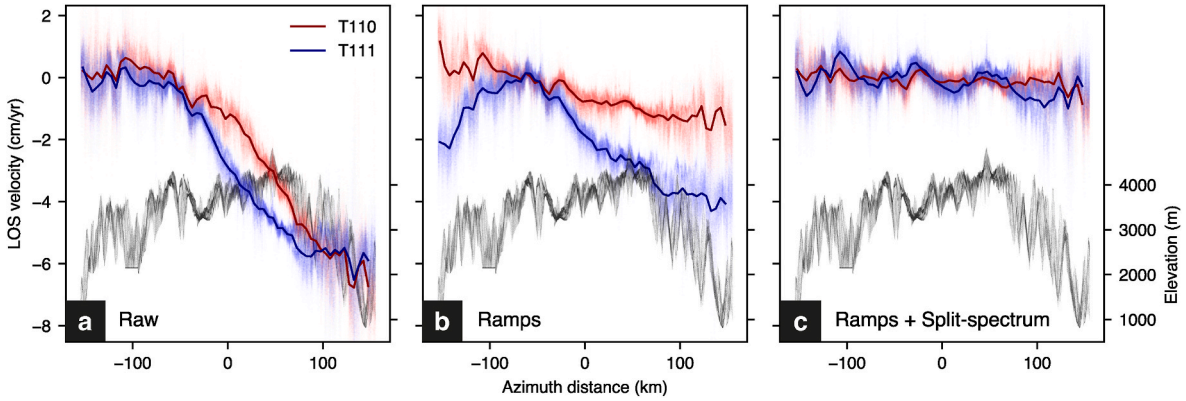

Fig. 7. Profiles of LOS velocity along the overlap between tracks 110 (in red) and 111 (in blue). The profile location is indicated on Fig. 4. Elevation profile is in black. (a) Raw time-series; (b) time-series after removal of a phase ramp only; (c) time-series after removal of a phase ramp and split-spectrum correction. (For interpretation of the references to color in this figure legend, the reader is referred to the Web version of this article.)

the case with the ramp removal strategy. Moreover, data separated by a short distance (with close azimuth distance, shown by color in Fig. 8b) displays sub-trends aligned on one-to-one relationship. This shows that at short scale, the agreement between both tracks is far better, of the order of 1–2 mm/yr. The split-spectrum procedure applied to time-series allows to reach a consistency on LOS velocity of about 0.31 cm/yr at large scale in coherent areas, but short scale features (~10 km) in the velocity maps are consistent within 0.1 cm/yr.

The high RMS misclosure subset show a much higher dispersion in general, even for the points close in space (Fig. 8c and d). However, the split-spectrum correction also strongly improves the consistency between the two tracks in this subset. The RMS of the velocity difference

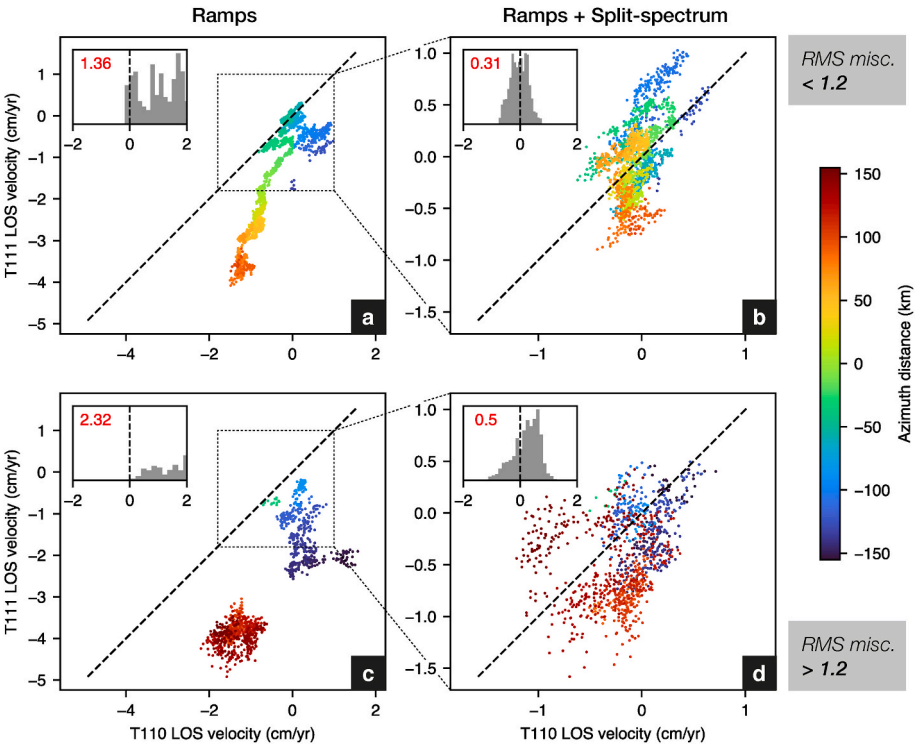

Fig. 8. Consistency analysis of the LOS velocity on the overlap between tracks 110 and 111. The LOS velocity of track 111 is plotted as a function of that of track 110, with color-coding corresponding to azimuth distance along the overlap. Panels a and c show the velocities from Fig. 7b, obtained from the time-series after removal of a phase ramp only. Panels b and d show the velocities from Fig. 7c, obtained from the time-series after removal of a phase ramp and split-spectrum correction. Panels a and b show velocities for points with associated RMS misclosure <1.2 rad. Panels c and d show velocities for points with associated RMS misclosure >1.2 rad. For each panel, the inset represents a histogram of the velocity difference between the two tracks, and the red value correspond to the RMS of the difference in cm/yr. (For interpretation of the references to color in this figure legend, the reader is referred to the Web version of this article.)

between the two tracks is reduced from 2.3 cm/yr with ramp removal only to 0.5 cm/yr with the IPS correction. The distribution of velocity difference is brought in the ±1 cm/yr interval although it is not exactly centered on zero. Finally, for these low-coherence areas, it is less clear that the consistency between the tracks increases at small spatial scales. This analysis confirms that not only the quality of the original InSAR time-series, but also the quality of the ionospheric corrections strongly depends on the interferometric coherence.

5.2. Variance analysis on time-series

We compute the square-root of semi-variograms on the time-series displacement maps masked for RMS misclosure >0.8 rad (T110 and T111) or > 1.0 rad (T119 and T499). In order to target specifically the spatial wavelength of ionospheric patterns, we extract a dispersion indicator σ_{50} from the variograms at a 50 km distance (examples in Fig. 2). We assume that this measurement represents mainly the contribution of ionospheric noise. This is justified by the large sensitivity of L-band SAR data to ionospheric disturbance, the latter being especially strong in equatorial regions, and empirically by the spatial patterns observed in the phase maps, typical of ionospheric signature.

The dispersion measurements for each acquisition of the four time-series are summarized in Fig. 9, for the different correction strategies shown throughout this study. The dispersion of raw time-series (grey bars) allows to compare the level of ionospheric perturbation of the different datasets, and confirms the more regular occurrence of strong perturbations in Ecuador (T110 and T111) than in Trinidad (T119) and Sumatra (T499). The simple ramp removal strategy (blue bars) appears to reduce, sometimes importantly, the dispersion of acquisitions. However, as noticed earlier, this improvement is very limited for acquisitions showing a large initial dispersion (i.e. mostly acquisitions with non-linear patterns). In contrast, the combination of split-spectrum correction and ramp removal (red bars) allows systematically to reduce the dispersion by at least a factor two with respect to the raw time-series. It is clear also that this strategy is the one leading to the more homogeneous residual amplitude between the different acquisitions (e.g. very clear for T110). This analysis highlight that the split-spectrum correction improvement is especially valuable for the acquisitions with high amplitude and spatially complex ionospheric perturbations. Moreover, based on our results, it appears that split-spectrum corrections inverted in time-series never increases the dispersion of the results (e.g. Fig. 2c). This correction could thus be applied in studies where ramp removal cannot be performed (e.g. for studies of large-scale continental motion). Yet, one should notice that using only the split-spectrum correction without ramp removal can leave out residual linear patterns for some acquisitions, such as 20070107 and 20080110 in track 119 (Fig. S5). These patterns may be due to orbital errors, and a further ramp removal improves the results.

The uncertainty on relative InSAR time-series increases with the spatial size of the signal of interest. To constrain the dependance of the uncertainty on distance, we compute the square-root of the semi-variogram, σ, for the four time-series computed in this study, after split-spectrum correction and ramp removal. We then convert them to an uncertainty on the relative velocity values as a function of distance, using (similarly to Parizzi et al., 2021):

$$\sigma_{velocity} = \frac{1}{\sqrt{N-2}} \frac{\sigma}{\sigma_{dates}} \tag{8}$$

where σ_{dates} is the standard deviation of the acquisition dates and N is the number of dates. This conversion gives an uncertainty in cm/yr as a function of distance, shown in Fig. 10. The uncertainties curves (Fig. 10) for the four tracks have similar shapes and values: the uncertainty

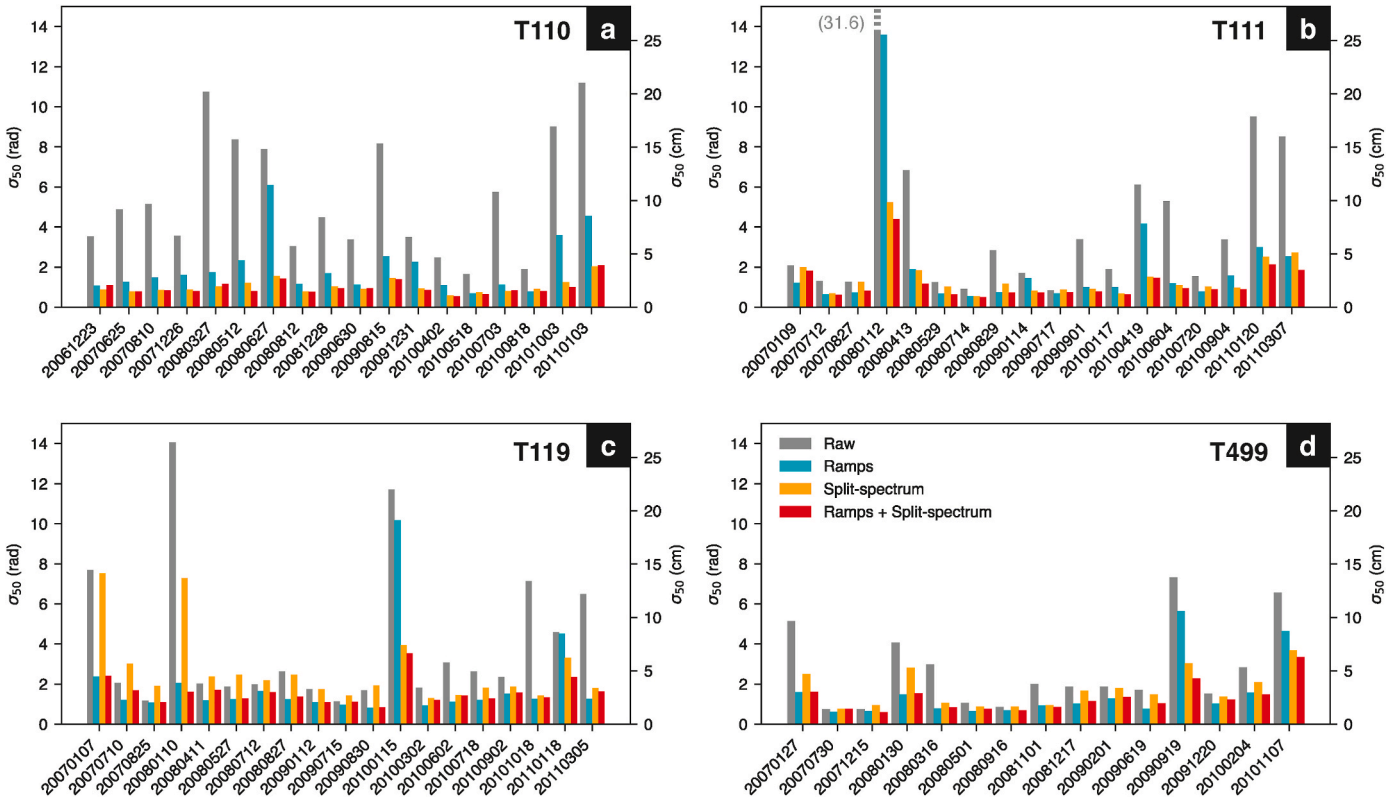

Fig. 9. Comparison of the square-root of the semivariogram at a 50 km distance (**σ50**) for the 4 tracks studied and with or without corrections. In grey: for raw time-series; in blue: for time-series after removal of a phase ramp only; in orange: for time-series after split-spectrum correction only; in red: for time-series after removal of a phase ramp and split-spectrum correction. (For interpretation of the references to color in this figure legend, the reader is referred to the Web version of this article.)

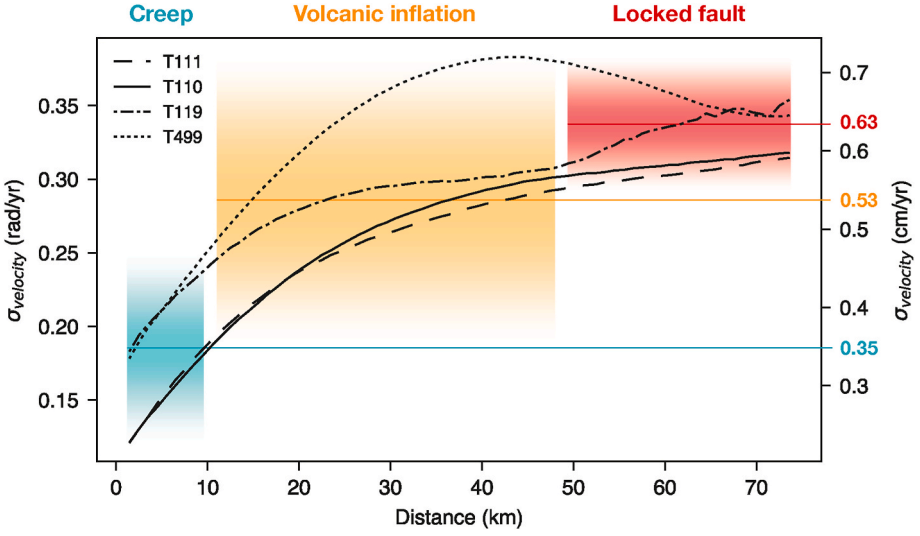

Fig. 10. Mean uncertainty on the velocity obtained from the linear fit of the time-series as a function of distance, after removal of a phase ramp and split-spectrum correction. Colored values on the right axis indicate the resulting uncertainties for spatial distances corresponding to three phenomena typically studied using InSAR (fault creep in blue, volcanic inflation in yellow, interseismic deformation on a locked fault in red). (For interpretation of the references to color in this figure legend, the reader is referred to the Web version of this article.)

increases until distances of ~50 km, where they reach a plateau around 0.6 cm/yr. The time-series of track 499 show a bump around 40 km distance that likely corresponds to residual ionospheric artifacts.

We delimited approximately three distance domains corresponding to the phenomena most studied using L-band InSAR: fault creep below 10 km, volcanic inflation between 10 and 50 km, and interseismic strain on a locked fault above 50 km. From the mean values of the uncertainty curves in these domains, we derive semi-quantitative empirical thresholds for the measurement of each of these phenomena with L-band InSAR data. These estimations apply for time-series in equatorial regions, with a number of acquisitions typical of the ALOS-PALSAR archive, i.e. 15 to 20 acquisitions in a 4-years time span. Fault creep can therefore be detected if it produces a LOS displacement greater than 0.35 cm/yr, whereas we can only expect to measure locked interseismic

motion larger than 0.63 cm/yr. This is higher than the deformation rates across the CCPP inferred by GNSS (0.3–0.5 cm/yr in LOS), and explains thus that this signal is still covered by time-series' noise. Volcanic inflation is in an intermediate situation, with a detection threshold around 0.5 cm/yr, largely exceeded by the Tungurahua inflation rates that we observe in this study.

6. Conclusion

Ionospheric perturbations can be a major source of noise in InSAR, especially using L-band data in equatorial regions. When trying to detect small ground motion using time-series analysis of InSAR data in such conditions, compensating this source of error becomes mandatory. In this study, we use the now widespread range split-spectrum technique to correct time-series of ALOS-PALSAR data in different equatorial contexts. As we deal with low to medium coherence datasets, we adapt the implementation of the technique in order to optimize signal-to-noise ratio, especially during multilooking, unwrapping, filtering, and time-series inversion steps. We use the time-series corrected using this procedure to demonstrate the efficiency of the ionospheric compensation, and to evaluate empirically the reached accuracy.

It turns out that the combination of the split-spectrum correction with ramp fitting and removal reduces drastically the impact of ionospheric noise on the time-series, even when almost all acquisitions are contaminated by ionosphere. A simple ramp removal approach is not sufficient for correcting efficiently the highly non-linear patterns often characterizing ionospheric perturbations at equatorial regions. Therefore, the split-spectrum procedure leads to a more significant improvement of these very disturbed acquisitions, and allows homogenizing of the spatial dispersion of the time-series. The square root of semivariograms at a 50 km distance is confined below 7 cm for all acquisitions after the correction, while it could reach 60 cm in the uncorrected time-series. As a result, we show that the corrected ALOS time-series can be used to probe the temporal behavior of the geophysical signals of interest.

From a geostatistical analysis, we derive an empirical accuracy for the LOS velocity measurement using such datasets, highlighting its dependence on spatial distance. From the typical ALOS-PALSAR archive, we show that deformation rates down to ~6 mm/yr at large distances (>50 km, such as interseismic strain accumulation) can be detected. Looking at small wavelength deformation, such as fault creep (<10 km), the detection threshold is around 3 mm/yr. Similar accuracy estimates are derived from the analysis of the overlapping data between two adjacent tracks in Ecuador. These values depend on interferometric coherence, as the ionospheric phase screen computation is very sensitive to phase noise. Other noise sources, such as DEM errors or residual tropospheric delay, contribute to this error, but to a lesser extent. Our estimates of accuracy are consistent with the residual error between GNSS and InSAR computed by Liang et al. (2018) and Liang et al. (2019) for ALOS-2 and Sentinel-1 time-series corrected using split-spectrum method, although the latter have been computed in areas characterized by larger interferometric coherence.

The velocity maps extracted from the corrected time-series enable tectonic creep and volcanic inflation to be accurately detected and measured in Ecuador, Trinidad and Sumatra. Yet, small amplitude and large-scale interseismic loading on a fault system in Ecuador could not be resolved despite the correction. Smaller uncertainties are expected for the next generation of L-band satellites (e.g. ALOS-2 or NISAR) due to orbit control and once a larger number of acquisitions over a longer time-span than for ALOS-PALSAR are acquired. Interseismic loading rates on faults located in densely vegetated equatorial regions will then be measured by InSAR.

CRediT authorship contribution statement

Léo Marconato: Data curation, Formal analysis, Investigation, Methodology, Software, Visualization, Writing – original draft. **Marie-Pierre Doin:** Conceptualization, Methodology, Software, Supervision, Validation, Writing – review & editing. **Laurence Audin:** Funding acquisition, Project administration, Resources, Supervision, Validation, Writing – review & editing. **Erwan Pathier:** Validation, Writing – review & editing.

Declaration of competing interest

The authors declare that they have no known competing financial interests or personal relationships that could have appeared to influence the work reported in this paper.

Data availability

Data will be made available on request.

Acknowledgements

The Editors and three anonymous reviewers are gratefully acknowledged for their valuable comments. This research was supported by the Centre National d'Études Spatiales (CNES), through the MONA project.

Appendix A. Supplementary data

Supplementary data to this article can be found online at https://doi.org/10.1016/j.srs.2023.100113.

References

Alvarado, A., Audin, L., Nocquet, J.M., Jaillard, E., Mothes, P., Jarrín, P., Segovia, M., Rolandone, F., Cisneros, D., 2016. Partitioning of oblique convergence in the Northern Andes subduction zone: Migration history and the present-day boundary of the North Andean Sliver in Ecuador. Tectonics 35, 1048–1065. https://doi.org/10.1002/2016TC004117.

Belcher, D.P., 2008. Theoretical limits on SAR imposed by the ionosphere. IET Radar. Sonar & Navigation 2, 435–448. https://doi.org/10.1049/iet-rsn:20070188.

Berardino, P., Fornaro, G., Lanari, R., Sansosti, E., 2002. A new algorithm for surface deformation monitoring based on small baseline differential SAR interferograms. IEEE Trans. Geosci. Remote Sensing 40, 2375–2383. https://doi.org/10.1109/TGRS.2002.803792.

Biggs, J., Wright, T., Lu, Z., Parsons, B., 2007. Multi-interferogram method for measuring interseismic deformation: Denali Fault, Alaska. Geophys. J. Int. 170, 1165–1179. https://doi.org/10.1111/j.1365-246X.2007.03415.x.

Blewitt, G., Hammond, W., Kreemer, C., 2018. Harnessing the GPS data explosion for interdisciplinary science. Eos 99. https://doi.org/10.1029/2018EO104623.

Brcic, R., Parizzi, A., Eineder, M., Bamler, R., Meyer, F., 2010. Estimation and compensation of ionospheric delay for SAR interferometry. In: 2010 IEEE International Geoscience and Remote Sensing Symposium. Presented at the IGARSS 2010 - 2010 IEEE International Geoscience and Remote Sensing Symposium. IEEE, Honolulu, HI, USA, pp. 2908–2911. https://doi.org/10.1109/IGARSS.2010.5652231.

Bürgmann, R., Rosen, P.A., Fielding, E.J., 2000. Synthetic aperture radar interferometry to measure Earth's surface topography and its deformation. Annu. Rev. Earth Planet Sci. 28, 169–209. https://doi.org/10.1146/annurev.earth.28.1.169.

Champenois, J., Baize, S., Vallee, M., Jomard, H., Alvarado, A., Espin, P., Ekström, G., Audin, L., 2017. Evidences of surface rupture associated with a low-Magnitude (Mw5.0) shallow earthquake in the Ecuadorian Andes. J. Geophys. Res. Solid Earth 122, 8446–8458. https://doi.org/10.1002/2017JB013928.

Champenois, J., Pinel, V., Baize, S., Audin, L., Jomard, H., Hooper, A., Alvarado, A., Yepes, H., 2014. Large-scale inflation of Tungurahua volcano (Ecuador) revealed by Persistent Scatterers SAR interferometry. Geophys. Res. Lett. 41, 5821–5828. https://doi.org/10.1002/2014GL060956.

Davidson, G.W., Bamler, R., 1999. Multiresolution phase unwrapping for SAR interferometry. IEEE Trans. Geosci. Rem. Sens. 37, 163–174. https://doi.org/10.1109/36.739150.

Dianala, J.D.B., Jolivet, R., Thomas, M.Y., Fukushima, Y., Parsons, B., Walker, R., 2020. The relationship between seismic and Aseismic slip on the Philippine fault on Leyte island: Bayesian modeling of fault slip and Geothermal subsidence. JGR Solid Earth 125. https://doi.org/10.1029/2020JB020052.

Doin, M.-P., Guillaso, S., Jolivet, R., Lasserre, C., Lodge, F., Ducret, G., Grandin, R., 2011. Presentation of the small baseline NSBAS processing chain on a case example: the Etna deformation monitoring from 2003 to 2010 using Envisat data. In: Presented at the Proceedings of the Fringe Symposium, ESA SP-697, pp. 3434–3437. Frascati, Italy.

Doin, M.-P., Lasserre, C., Peltzer, G., Cavalié, O., Doubre, C., 2009. Corrections of stratified tropospheric delays in SAR interferometry: Validation with global atmospheric models. J. Appl. Geophys. 69, 35–50. https://doi.org/10.1016/j.jappgeo.2009.03.010.

Doin, M.-P., Cheiab, A., Thollard, F., 2023. Strategy used for phase unwrapping in the NSBAS MT-InSAR chain. In: Presented at the IGARSS 2023 IEEE International Geoscience and Remote Sensing Symposium. IEEE, Pasadena, CA, USA, pp. 8210–8213. https://doi.org/10.1109/IGARSS52108.2023.10283158.

Ducret, G., Doin, M.-P., Grandin, R., Lasserre, C., Guillaso, S., 2014. DEM corrections before unwrapping in a small baseline strategy for InSAR time series analysis. Geosci. Rem. Sens. Lett. IEEE 11, 696–700. https://doi.org/10.1109/LGRS.2013.2276040.

Dzurisin, D., 2003. A comprehensive approach to monitoring volcano deformation as a window on the eruption cycle: volcano DEFORMATION. Rev. Geophys. 41 https://doi.org/10.1029/2001RG000107.

European Space Agency, 2022. Airbus. https://doi.org/10.5270/ESA-c5d3d65. Copernicus DEM.

Fattahi, H., Simons, M., Agram, P., 2017. InSAR time-series estimation of the ionospheric phase delay: an extension of the split range-spectrum technique. IEEE Trans. Geosci. Rem. Sens. 55, 5984–5996. https://doi.org/10.1109/TGRS.2017.2718566.

Gatelli, F., Monti Guamieri, A., Parizzi, F., Pasquali, P., Prati, C., Rocca, F., 1994. The wavenumber shift in SAR interferometry. IEEE Trans. Geosci. Rem. Sens. 32, 855–865. https://doi.org/10.1109/36.298013.

Global Volcanism Program, 2013. Report on Tungurahua (Ecuador). Bull. Glob. Volcanism Netw. 38 https://doi.org/10.5479/si.GVP.BGVN201303-352080.

Gomba, G., Parizzi, A., De Zan, F., Eineder, M., Bamler, R., 2016. Toward operational compensation of ionospheric effects in SAR interferograms: the split-spectrum method. IEEE Trans. Geosci. Rem. Sens. 54, 1446–1461. https://doi.org/10.1109/TGRS.2015.2481079.

Gray, A.L., Mattar, K.E., Sofko, G., 2000. Influence of ionospheric electron density fluctuations on satellite radar interferometry. Geophys. Res. Lett. 27, 1451–1454. https://doi.org/10.1029/2000GL000016.

Guillaso, S., Lasserre, C., Doin, M., Cavalié, O., Sun, J., Peltzer, G., 2008. InSAR Measurement of Interseismic Strain in Areas of Low Coherence: Example across the Haiyuan Fault (Gansu, China) Using a Local InSAR Adaptive Range Filter. Presented at the Eur. Geosci. Union, Vienna.

Higgins, M., La Femina, P.C., Weber, J.C., Geirsson, H., Ryan, G.A., Wauthier, C., 2021. Strain partitioning and interseismic fault behavior along the Caribbean-South American transform plate boundary. Tectonics 40. https://doi.org/10.1029/2021TC006740.

Ho Tong Minh, D., Hassen, R., Doin, M.P., Pathier, E., 2022. Advanced methods in time series InSAR. In: Surface Displacement Measurement from Remote Sensing Images. Wiley. https://doi.org/10.1002/9781119986843.

Ito, T., Gunawan, E., Kimata, F., Tabei, T., Simons, M., Meilano, I., Agustan Ohta, Y., Nurdin, I., Sugiyanto, D., 2012. Isolating along-strike variations in the depth extent of shallow creep and fault locking on the northern Great Sumatran Fault: along-strike variations on the GSF. J. Geophys. Res. 117, 10.1029/2011JB008940.

Jolivet, R., Agram, P.S., Lin, N.Y., Simons, M., Doin, M., Peltzer, G., Li, Z., 2014. Improving InSAR geodesy using global atmospheric models. J. Geophys. Res. Solid Earth 119, 2324–2341. https://doi.org/10.1002/2013JB010588.

Jolivet, R., Grandin, R., Lasserre, C., Doin, M.-P., Peltzer, G., 2011. Systematic InSAR tropospheric phase delay corrections from global meteorological reanalysis data. Geophys. Res. Lett. 38, 10.1029/2011GL048757.

Jouanne, F., Audemard, F.A., Beck, C., Van Welden, A., Ollarves, R., Reinoza, C., 2011. Present-day deformation along the El Pilar Fault in eastern Venezuela: evidence of creep along a major transform boundary. J. Geodyn. 51, 398–410. https://doi.org/10.1016/j.jog.2010.11.003.

Jung, H.-S., Lee, D.-T., Lu, Z., Won, J.-S., 2013. Ionospheric correction of SAR interferograms by Multiple-aperture interferometry. IEEE Trans. Geosci. Rem. Sens. 51, 3191–3199. https://doi.org/10.1109/TGRS.2012.2218660.

Kelley, M., 2009. The Earth's Ionosphere. Elsevier.

Li, B., Wang, Z., An, J., Zhang, B., Geng, H., Ma, Y., Li, M., Qian, Y., 2020. Ionospheric phase compensation for InSAR measurements based on the Faraday rotation inversion method. Sensors 20, 6877. https://doi.org/10.3390/s20236877.

Liang, C., Agram, P., Simons, M., Fielding, E.J., 2019. Ionospheric correction of InSAR time series analysis of C-band Sentinel-1 TOPS data. IEEE Trans. Geosci. Rem. Sens. 57, 6755–6773. https://doi.org/10.1109/TGRS.2019.2908494.

Liang, C., Liu, Z., Fielding, E.J., Burgmann, R., 2018. InSAR time series analysis of L-band wide-swath SAR data acquired by ALOS-2. IEEE Trans. Geosci. Rem. Sens. 56, 4492–4506. https://doi.org/10.1109/TGRS.2018.2821150.

Liao, H., Meyer, F.J., Scheuchl, B., Mouginot, J., Joughin, I., Rignot, E., 2018. Ionospheric correction of InSAR data for accurate ice velocity measurement at polar regions. Remote Sensing of Environment 209, 166–180. https://doi.org/10.1016/j.rse.2018.02.048.

López-Quiroz, P., Doin, M.-P., Tupin, F., Briole, P., Nicolas, J.-M., 2009. Time series analysis of Mexico City subsidence constrained by radar interferometry. J. Appl. Geophys. 69, 1–15. https://doi.org/10.1016/j.jappgeo.2009.02.006.

Meyer, F.J., Chotoo, K., Chotoo, S.D., Huxtable, B.D., Carrano, C.S., 2016. The influence of equatorial scintillation on L-band SAR image quality and phase. IEEE Trans. Geosci. Rem. Sens. 54, 869–880. https://doi.org/10.1109/TGRS.2015.2468573.

Morales Rivera, A.M., Amelung, F., Mothes, P., 2016. Volcano deformation survey over the Northern and Central Andes with ALOS InSAR time series. Geochem. Geophys. Geosyst. 17, 2869–2883. https://doi.org/10.1002/2016GC006393.

Nocquet, J.-M., Villegas-Lanza, J.C., Chlieh, M., Mothes, P.A., Rolandone, F., Jarrin, P., Cisneros, D., Alvarado, A., Audin, L., Bondoux, F., Martin, X., Font, Y., Régnier, M., Vallée, M., Tran, T., Beauval, C., Maguiña Mendoza, J.M., Martinez, W., Tavera, H., Yepes, H., 2014. Motion of continental slivers and creeping subduction in the northern Andes. Nature Geosci 7, 287–291. https://doi.org/10.1038/ngeo2099.

Parizzi, A., Brcic, R., De Zan, F., 2021. InSAR performance for large-scale deformation measurement. IEEE Trans. Geosci. Rem. Sens. 59, 8510–8520. https://doi.org/10.1109/TGRS.2020.3039006.

Pi, X., Freeman, A., Chapman, B., Rosen, P., Li, Z., 2011. Imaging ionospheric inhomogeneities using spaceborne synthetic aperture radar. J. Geophys. Res. 116, 10.1029/2010JA016267.

Pinel-Puyssegur, B., Michel, R., Avouac, J.-P., 2012. Multi-link InSAR time series: enhancement of a wrapped interferometric Database. IEEE J. Sel. Top. Appl. Earth Observations Remote Sensing 5, 784–794. https://doi.org/10.1109/JSTARS.2012.2196758.

Pousse Beltran, L., Pathier, E., Jouanne, F., Vassallo, R., Reinoza, C., Audemard, F., Doin, M.P., Volat, M., 2016. Spatial and temporal variations in creep rate along the El Pilar fault at the Caribbean-South American plate boundary (Venezuela), from InSAR. J. Geophys. Res. Solid Earth 121, 8276–8296. https://doi.org/10.1002/2016JB013121.

Raucoules, D., de Michele, M., 2010. Assessing ionospheric influence on L-band SAR data: implications on Coseismic displacement measurements of the 2008 Sichuan earthquake. Geosci. Rem. Sens. Lett. IEEE 7, 286–290. https://doi.org/10.1109/LGRS.2009.2033317.

Tong, X., Sandwell, D.T., Schmidt, D.A., 2018. Surface creep rate and Moment accumulation rate along the Aceh segment of the Sumatran Fault from L-band ALOS-1/PALSAR-1 observations. Geophys. Res. Lett. 45, 3404–3412. https://doi.org/10.1002/2017GL076723.

Weber, J.C., Dixon, T.H., DeMets, C., Ambeh, W.B., Jansma, P., Mattioli, G., Saleh, J., Sella, G., Bilham, R., Pérez, O., 2001. GPS estimate of relative motion between the Caribbean and South American plates, and geologic implications for Trinidad and Venezuela. Geol. 29, 75. https://doi.org/10.1130/0091-7613(2001)029<0075:GEORMB>2.0.CO;2.